Available online at www.sciencedirect.com
ScienceDirect
Trans. Nonferrous Met. Soc. China 35(2025) 1292−1305
Transactions of Nonferrous Metals Society of China
www.tnmsc.cn

Preparation of $(NH_4)_2V_6O_{16}·1.5H_2O$ nanoribbons and their application in aqueous ammonium-ion batteries

Lin XING[1,2], Wei ZHOU[1], Kai-xiong XIANG[2], Wei-na DENG[1], Liang CHEN[1], Hai ZHU[1], Han CHEN[1]

1. Hunan Key Laboratory of Applied Environmental Photocatalysis, Changsha University, Changsha 410022, China;
2. College of Liling Ceramic, Hunan University of Technology, Zhuzhou 412007, China

Received 28 July 2023; accepted 3 June 2024

Abstract: To construct high-performance aqueous ammonium-ion full batteries, $(NH_4)_2V_6O_{16}·1.5H_2O$ (NVO) nanoribbon cathodes were prepared by pH-regulated hydrothermal synthesis. Anodes were prepared by growing the active material polyaniline (PANI) on carbon cloth. The assembled NVO//PANI full cells exhibit a reversible capacity of 109.5 mA·h/g at a current density of 1.0 A/g and a high energy density of 23 W·h/kg. The ammonium-ion intercalation/extraction mechanism is primarily governed by the pseudocapacitance behavior. These results indicate that NVO is a potential candidate as a cathode material for aqueous ammonium-ion batteries.

Key words: $(NH_4)_2V_6O_{16}·1.5H_2O$; cathode; ammonium-ion battery; carbon cloth; electrochemical performance

1 Introduction

Lithium-ion batteries are currently the most extensively utilized energy storage devices. However, concerns regarding their safety and the limited resources of precious metals, including lithium, have prompted the development of new battery systems [1−3]. Since the discovery of lithium ions as excellent charge carriers, the majority of research on charge carriers has focused on metal cations such as Na^+ [4], K^+ [5], Zn^{2+} [6], Mg^{2+} [7], Ca^{2+} [8], and Al^{3+} [9]. For instance, WESSELLS et al [10] reported the use of the Prussian blue analog $KM[Fe(CN)_6]$ (M=Cu or Ni) as a cathode material in aqueous ammonium-ion batteries. Notably, Prussian blue analogues [11], Ti_3C_2 MXene [12], organic solids [13], and metal oxides, such as titanic acid [14], V_2O_5 [15], and MoO_3 [16], have been widely studied in the field of ammonium (NH_4^+) ion storage chemistry. WU et al [17] reported that $(NH_4)_{1.47}Ni[Fe(CN)_6]_{0.88}$ could be used as a cathode when paired with 3,4,9,10-perylenetetracarboxylicdiimide as the anode in ammonium-ion full cells. Furthermore, the hydrogen bond chemistry involving NH_4^+ ions and V_2O_5 has been investigated, and a monkey-bar swing mechanism has been proposed to illustrate the presence of numerous chemical bonds between the ammonium ions and the electrode host [15], Ammonium ions have garnered increasing research attention for aqueous batteries due to their abundance, low density (minimum molar mass of 18 g/mol), and good diffusion capacity [18]. These properties mean that ammonium ions are particularly suitable for preparing devices with ultrafast dynamics and high power densities. Nevertheless, the systematic exploration of ammonium-ion batteries is still in its infancy, and there are main challenges in preparing high-performance ammonium-ion full batteries: (1) The large size and peculiar tetrahedral structure of the

Corresponding author: Wei ZHOU, Tel: +86-15974277940, E-mail: zhouwei_csu@163.com;
Han CHEN, Tel: +86-13786350206, E-mail: lzdxnchh@126.com
DOI: https://doi.org/10.1016/S1003-6326(24)66749-X

ammonium ions limit the specific capacity of cathode materials due to the lack of suitable ammonium-ion hosts with large structures; (2) The development of anode materials with easily tailorable properties and high structural stability for NH_4^+ ions is extremely difficult; (3) The slow redox reaction kinetics and poor electrode conductivity of NH_4^+ ions significantly limit the electrochemical performance of ammonium-ion full cells, resulting in a relatively low rate capability and high polarization. Therefore, the development of new anodes and NH_4^+ ion cathodes with high conductivity, high specific capacity, and good rate performance is fundamental for constructing high-performance ammonium-ion full cells.

Layered transition-metal oxides have attracted considerable attention in recent decades due to their two-dimensional channels, which facilitate the diffusion of various ions and adapt to volume changes during the intercalation process [19]. For example, WAN et al [20] developed $NaV_3O_8·1.5H_2O$ (NVO) nanoribbons as an advanced electrode material for zinc-ion batteries. The interlayer structure composed of water and sodium ions acted as a series of pillars, which stabilized the vanadium oxide layers during the charge/discharge process. Owing to the co-intercalation of H^+ and Zn^{2+} ions, this layered $NaV_3O_8·1.5H_2O$ electrode material exhibited a high reversible capacity and a long cycle life. Therefore, it can be expected that materials with a lamellar structure can also be used as host materials for the intercalation of ammonium ions. However, studies on electrode materials for ammonium-ion batteries have rarely been conducted to date. Moreover, a comprehensive understanding of the charge storage mechanism is also required. Negative electrodes are crucial for the construction of full batteries, and ideal anode materials should exhibit a high capacity to accommodate NH_4^+ ions, a fast redox reaction kinetics, and a suitable redox potential (higher than the potential of the hydrogen precipitation reaction but lower than the potential of the oxygen precipitation reaction in the electrolyte). Furthermore, electrode materials should be easily processable. Notably, polyaniline is a conductive polymer with pseudocapacitive properties, which offers numerous advantages, such as tunable morphology, good environmental stability, and excellent conductivity. Additionally, the synthesis of polyaniline is simple and facile. To achieve composite electrodes with large capacitance and good flexibility, the distribution and morphology of the active material on flexible substrates must be optimized.

In this study, the NVO nanoribbons were successfully synthesized by a simple hydrothermal method, and the effect of the growth solution pH on the structural changes and ammonium ion storage properties of the NVO cathodes was systematically investigated. These aqueous secondary batteries based on abundant ammonium ions, stable ammonium vanadate cathodes, and polyaniline (PANI) anodes offer new perspectives for large-scale and rapid energy storage applications.

2 Experimental

2.1 Synthesis of NVO

NVO was synthesized via a hydrothermal method. Briefly, NH_4VO_3 (0.5 g) was dissolved in deionized water (25 mL), and the obtained solution was magnetically stirred for 30 min. The pH of the solution was adjusted to be 1.5, 2, 3, and 4 by adding 0.5, 0.4, 0.3, and 0.2 mL of H_3PO_4, respectively. The NOV samples prepared with these solutions are denoted as NVO-1.5, NVO-2, NVO-3, and NVO-4, respectively. The mixtures were then transferred to a Teflon-lined stainless-steel autoclave for the hydrothermal reaction, which was performed at 130 °C for 72 h. The resulting precipitates were washed three times with deionized water and ethanol and then dried at 60 °C for 12 h to obtain the NVO powders.

2.2 Synthesis of PANI

Carbon cloth (CC) was immersed in 68% HNO_3 for 12 h and then washed with deionized water. The CC was then further cleaned using an ultrasonic cleaner for 30 min. Aniline was electropolymerized on the CC by cyclic voltammetry (CV) using a solution containing aniline (0.5 mol/L) and H_2SO_4 (0.1 mol/L) in the potential window from −0.5 to 1.5 V at a scan rate of 10 mV/s. Electrochemical experiments were conducted on three-electrode devices using a carbon wafer with 18 mm in diameter as the substrate, a platinum electrode as the counter electrode, and a saturated calomel electrode as the reference electrode.

Detailed information on the materials characterization and electrochemical measurements are described in Sections 1 and 2 in Supporting Information.

3 Results and discussion

3.1 Phase structure and chemical component analysis

The X-ray diffraction (XRD) patterns of the NVO products prepared at various pH values are shown in Fig. 1. All diffraction peaks can be indexed to the monoclinic crystal system of NVO (PDF# 51-0376). No characteristic peaks corresponding to impurities were detected, and the NVO crystal structures obtained from the solutions with different pH values did not show any significant changes. With decreasing pH, a slight increase in the intensity of the main (002), (110), (204), (112), and (020) peaks was observed, indicating an increase in crystallinity.

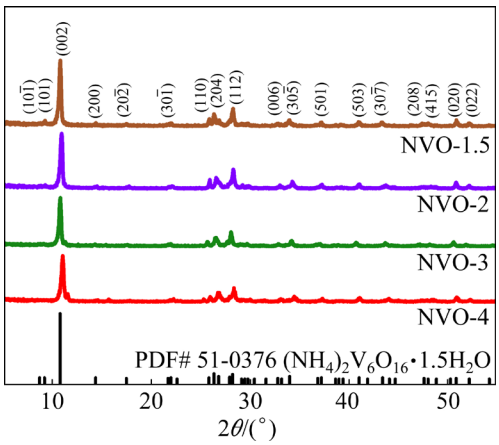

Fig. 1 XRD patterns of NVO-1.5, NVO-2, NVO-3, and NVO-4

The X-ray photoelectron spectroscopy (XPS) analysis of NVO-2 is shown in Fig. 2. Figure 2(a) demonstrates that NVO-2 is composed of N, O, and V elements. Furthermore, Fig. 2(b) shows that the V 2p peak can be deconvoluted into two peaks at 517.2 and 516.5 eV, which are attributed to V^{5+} and a small amount of V^{4+}, respectively. The N 1s peaks at 400.1 and 401.4 eV (Fig. 2(c)) can be assigned to the pure N—H bonds and N—H bonds with the V_3O_8 structure, respectively. Furthermore, the O 1s spectrum (Fig. S1 in Supporting Information) can be deconvoluted into three strong peaks centered at 530.3, 531.7, and 532.7 eV, which correspond to the V—O bonds between the NH_4^+ ions and the V—O layers, the —N—H···O bonds between the NH_4^+ ions and the water molecules, and the H—O bonds in the water molecules, respectively.

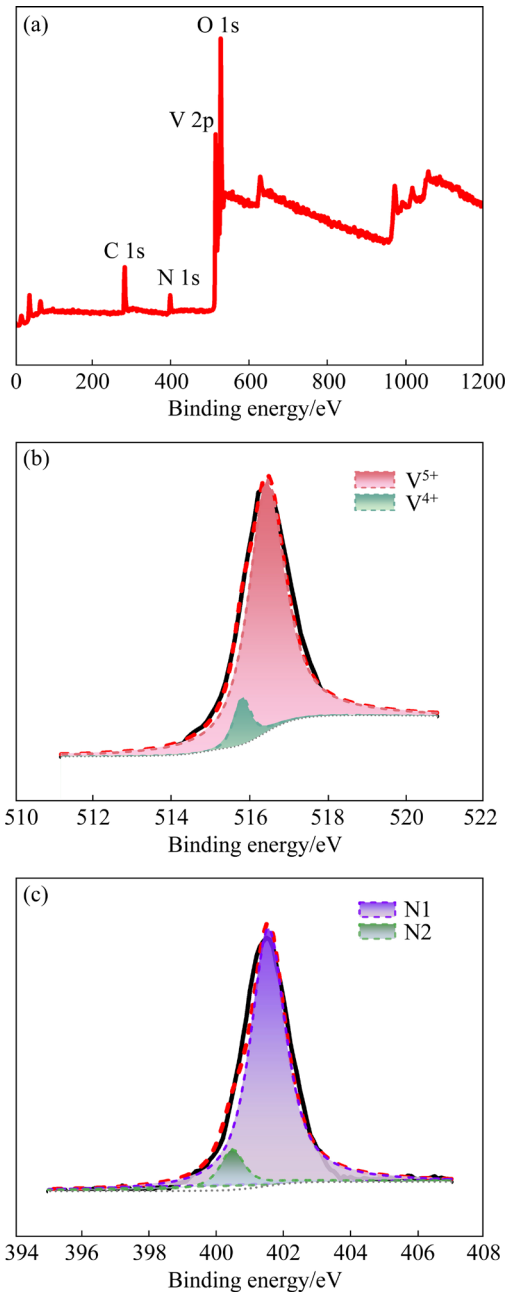

Fig. 2 XPS spectrum (a) and high-resolution V 2p (b) and N 1s (c) XPS spectra of NVO-2

The morphologies of the NVO samples prepared at different pH values were characterized by scanning electron microscopy (SEM) (Fig. 3(a) and Figs. S2(a)–(c) in Supporting Information). NVO-1.5 exhibited ribbon-like nanostructures with widths ranging from 40 to 380 nm, thicknesses ranging from 10 to 30 nm, and lengths between 0.1 and 3 μm. With increasing pH from 1.5 to 3, the

dimensions of the NVO nanoribbons did not change significantly. NVO-4 was found to exhibit irregular grains and nanoribbons. Figure 3(c) shows the selected area electron diffraction (SAED) pattern of NVO-2, which corresponded to the red region in the high-resolution transmission electron microscopy (HRTEM) image shown in Fig. 3(b). The measured lattice spacing values of 0.634 and 0.342 nm are consistent with those expected for the (200) and (110) planes of monoclinic NVO-2, respectively. The SAED patterns of all NVO nanoribbons exhibit clear single-crystal features (Fig. 3(c) and Fig. S2(j−l) in Supporting Information). The scanning transmission electron microscopy (STEM) and elemental mapping images of the NVO-2 nanoribbons show uniform distributions of V, N, and O elements (Fig. 3(d)). These results indicate that the monoclinic NVO crystals exhibit a distinct anisotropic growth and a uniform energy-band structure without any defects or dislocations.

The thermodynamic and kinetic states during crystal growth significantly influence the structure of the nanocrystals [21]. The synthesis reaction for the NVO nanoribbons is as follows:

$$6NH_4VO_3+H_3PO_4=(NH_4)_2V_6O_{16}\cdot 1.5H_2O+2NH_3+0.5H_2O+(NH_4)_3PO_4 \quad (1)$$

This reaction involves the dissociation of ammonium metavanadate into NH_4^+ and VO_3^- ions in an aqueous solution [21]. At elevated temperatures, the metavanadate groups start to associate to form a chain of VO_4 tetrahedra, which are linked together by common angles. As the reaction progresses, the tetrahedral chains transform into VO_5 square pyramids and VO_6 octahedra. At this stage, the VO_5 and VO_6 structural units are connected by common edges to form V_3O_8 layers [8]. The NH_4^+ cations and H_2O molecules are located in the interlayer spaces and interact with the V_3O_8 layers through N—H···O and OH—H···O bonds, respectively. The electrical attraction and hydrogen-bonding interactions between the sheets lead to the self-assembly and packing of the monoclinic NVO nanoribbons. The interconnectivity of NVO through bonds gives rise to a structure with enhanced rigidity, which improves the structural stability of the material during electrochemical cycling.

Based on the experimental results obtained herein, it can be concluded that adjusting the pH of the growth solution is an effective method for controlling the structure and morphology of ammonium vanadate. The addition of H_3PO_4 may play a significant role in the nucleation and growth of crystals by controlling the interfacial tension or surface free energy. When H_3PO_4 is added in a dropwise manner to the growth suspension, the local H^+ concentration at the nanocrystal surface changes, resulting in a significant variation in the surface free energy of each crystal plane. Facets that exhibit fast growth due to their higher free energies may exhibit anomalous growth characteristics, which results in an additional growth anisotropy. Moreover, the addition of H_3PO_4 can balance the growth rate of different crystal planes.

3.2 Electrochemical performance

The ammonium-ion storage performance of NVO was evaluated using assembled coin cells at various current densities. Figure 4(a) shows the cycling stability of the NVO electrodes at a current density of 0.5 A/g. Among the four NVO-based devices, the one that utilized NVO-2 exhibited the highest initial discharge capacity (177.7 mA·h/g) and the best cycling stability, with a specific discharge capacity of 101.2 mA·h/g after 100 cycles. During cycling, numerous NH_4^+ ions are irreversibly released into the intermediate layer of the main

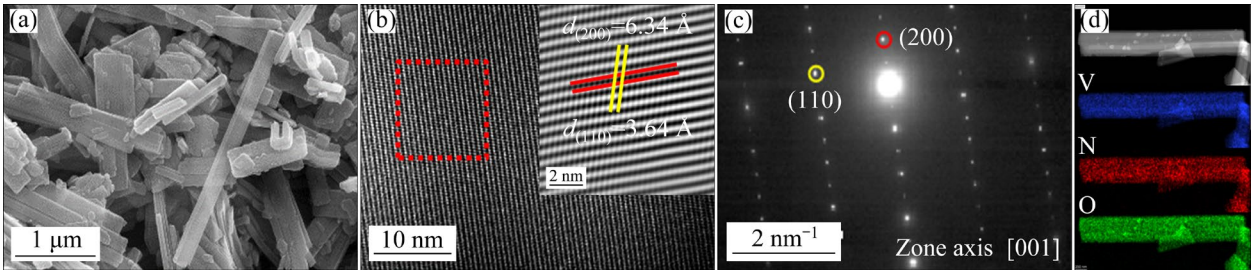

Fig. 3 SEM image (a) and HRTEM image (b) of NVO-2; SAED pattern (c) corresponding to red area depicted in (b), and STEM image showing energy-dispersive X-ray spectroscopy mapping images of N, V, and O (d)

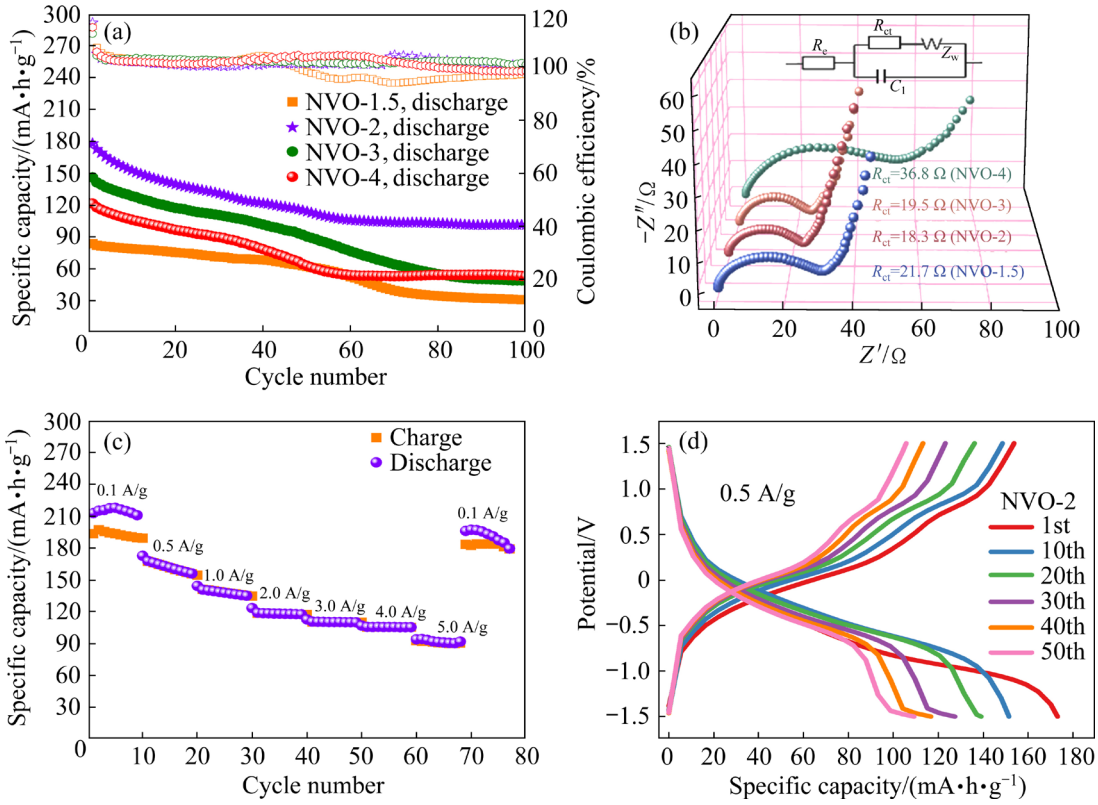

Fig. 4 Electrochemical properties of NVO for NH_4^+ ions: (a) Cyclic performance of NVO-2 with $(NH_4)_2SO_4$ electrolyte (1 mol/L) at 0.5 A/g over 100 cycles; (b) Nyquist plots of NVO-1.5, NVO-2, NVO-3, and NVO-4; (c) Rate performance; (d) Charge–discharge curves for different cycles

material, causing damage to the crystal structure. The interlayer structure is not fully recovered after undergoing a complete cycle, resulting in a reduction in capacity. This phenomenon has also been reported in previous studies [22,23].

Figure 4(b) depicts the Nyquist plots of NVO-1.5, NVO-2, NVO-3, and NVO-4 in the frequency range from 0.01 Hz to 100 kHz. The Nyquist plots are composed of two distinct regions: a high-frequency arc and a low-frequency oblique line. Compared with the NVO-1.5, NVO-3, and NVO-4 electrodes, the NVO-2 electrode presents a smaller semicircle in the high-frequency region and a line with a higher gradient in the low-frequency region. The real intercept (Z) represents the combined electrolyte ionic resistance (R_e) in the Nyquist plots. Notably, NVO-1.5, NVO-2, NVO-3, and NVO-4 exhibit similar R_e values in the as-prepared ammonium-ion batteries, which indicates that the intrinsic resistance of the substrate and the contact resistance at the interface between the active material and the current collector in these batteries are also similar. A semicircle, which is associated with the charge transfer resistance (R_{ct}) induced by the Faraday reaction, can be seen in the high-frequency part of the Nyquist plot [24] Moreover, the slope of this curve, which is known as the Warburg resistance (Z_w), is determined by the frequency-dependent diffusion and transport of the ions within the electrolyte, which moves toward the electrode surface. Based on the circuit shown in Fig. 4(b), it can be concluded that NVO-2 exhibits a similar R_e value as that of the NVO-1.5, NVO-3, and NVO-4 solutions, as well as the lowest R_{ct} and Z_w values among the four NVO solutions.

Figure 4(c) shows the rate capability of NVO-2. The average specific discharge capacities were found to be 212.7, 172.5, 144.2, 123.3, 110.1, 105.4, and 91.4 mA·h/g at current densities of 0.1, 0.5, 1.0, 2.0, 3.0, 4.0, and 5.0 A/g, respectively. The reversible capacity immediately recovered to a value of 195.9 mA·h/g as the current density returned to 0.1 A/g, indicating good tolerance toward the rapid de-insertion of NH_4^+ ions. Figure 4(d) illustrates the charge–discharge curves of the NVO-2 electrode at a current density of

0.5 A/g in different cycles. The discharge profiles exhibit an inclined voltage platform within the voltage range from −1.1 to 0.1 V, while the charging curves present two distinct voltage plateaus in the ranges from −0.55 to 0.2 V and from 0.7 to 0.9 V. The initial charge/discharge (de-insertion/ insertion) capacities were found to be 156.0 and 174.4 mA·h/g, respectively, with a Coulombic efficiency of 89.5%.

To investigate the electrochemical kinetics of the NVO cathodes, CV tests were performed at scanning rates ranging from 0.2 to 1.0 mV/s (Fig. 5(a)). Three reduction peaks at around 0.79, 0.47, and 0.1 V are observed in the anodic scan of the CV curves, indicating that the NH_4^+ ions undergo a multistep electrochemical intercalation process [25]. This finding is consistent with the observed charge–discharge curves. However, only two oxidation peaks at approximately 0.25 and −0.53 V can be observed in the anodic scan, indicating the occurrence of an irreversible phase transition [26] After the initial cycle, all CV curves overlap, demonstrating highly reversible NH_4^+ insertion and extraction processes. With increasing scan rate, the redox peaks gradually become broader, while the CV profiles remain unchanged. The charge transfer behavior can be determined by considering the relationship between the measured current (I) and the scan rate (v):

$$I=av^b \quad (2)$$

where a and b are adjustable parameters. The value of b can range from 0.5 (for a diffusion-controlled process) to 1 (for a capacitive process). The b values of Peaks 1−4 are calculated to be 0.88, 0.82, 0.84, and 0.80 (see Fig. 5(b)). This indicates that the kinetics of the ammonium ions in the NVO-2 electrode is predominantly governed by capacitive processes and only slightly affected by diffusion processes.

To analyze the relative contributions of the diffusion-controlled and capacitive processes from a quantitative perspective, the following relationship can be used:

$$I=k_1v+k_2v^{1/2} \quad (3)$$

where k_1v represents the contribution of the capacitive processes and $k_2v^{1/2}$ represents the contribution of the diffusion-controlled processes. The contributions of the two different charge storage mechanisms are illustrated in Fig. S3(a) in Supporting Information. The results indicate that the contribution of the capacitive processes increases from 88% to 96% with increasing scan rate from 0.2 to 1.0 mV/s. These values are higher than those observed for the other samples (83% for NVO-1.5, 72% for NVO-3, and 80% for NVO-4, as shown in Figs. S3(b–d) in Supporting Information). The predominant contribution of the capacitive processes is a key factor enabling fast reaction kinetics and high-speed performance.

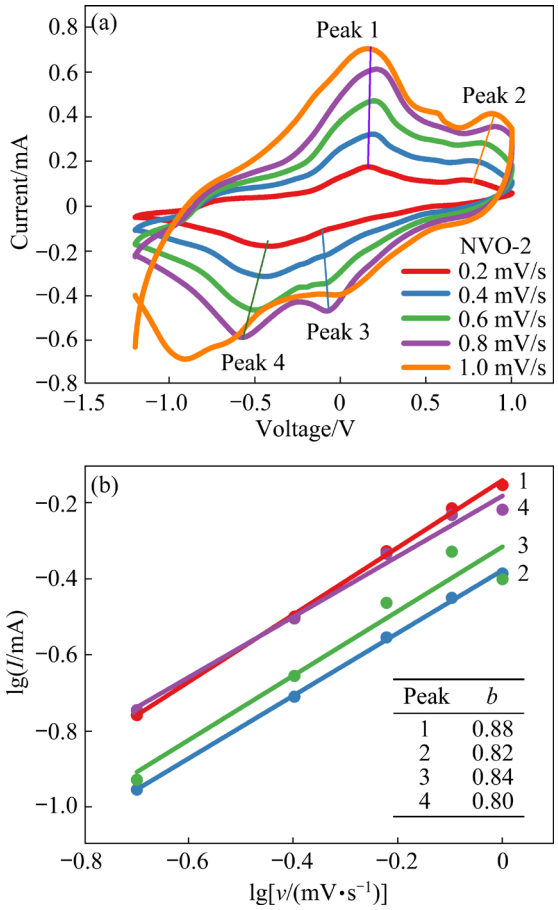

Fig. 5 CV curves at various scan rates (a) and lg I plotted against lg v (b)

3.3 Reaction mechanism

The correlation between the electrochemical behavior and structural evolution of NVO-2 was further investigated via ex-situ techniques, including XRD, Fourier-transform infrared (FTIR) spectroscopy, and XPS under different discharge/charge conditions. Notably, the ex-situ XRD patterns (Fig. 6(b)) only indicate small differences in the discharge/charge processes. Figure 6(c) illustrates that from Point a to Point c during the discharge process, the (002) peak shifts from 11.08° to 10.84°. This shift is accompanied by an increase

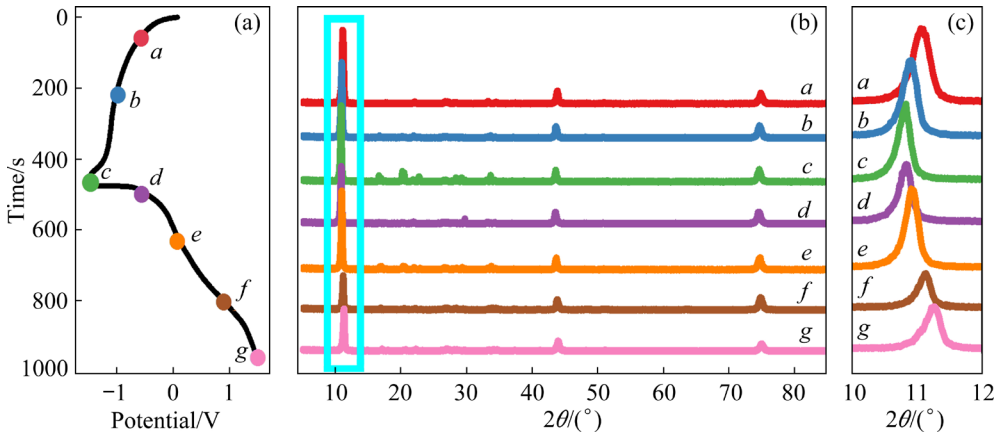

Fig. 6 Typical galvanostatic charge/discharge (GCD) profiles of electrodes (a) and ex-situ XRD patterns (b, c)

in the interlayer spacing from 7.98 to 8.15 Å and a volumetric expansion of approximately 2%, suggesting the introduction of NH_4^+ ions into the host lattice. Conversely, during the charging process from Point *d* to Point *g* (see Fig. 6(c)), the (002) peak shifts back to 11.26°, indicating a slight decrease in the interlayer spacing from 8.15 to 7.85 Å and a corresponding volumetric shrinkage of 3.8%. These results indicate the extraction of NH_4^+ ions from NVO-2. The cell volume shrinks slightly in the fully charged state due to the release of the NH_4^+ ions from the lattice structure of NVO-2.

Furthermore, the ex-situ FTIR spectroscopy measurements were performed to evaluate the structural variations of NVO-2 in different states (see Fig. 7). The two bands detected at 3142 and 1630 cm^{-1} can be attributed to the stretching vibration of the O—H bonds and the bending vibration of the H—O—H bonds, respectively, indicating the presence of crystalline water molecules within the structure. The broad bands observed at 3140 and 1404 cm^{-1} can be ascribed to the asymmetric stretching vibrations and symmetric bending vibrations of the N—H bonds in NH_4^+ ions, respectively. As the system discharges from the initial state (Point *a*) to Point *c*, the intensities of these two bands increase. However, during the charging process, as the system transitions to Point *g*, these intensities decrease. This behavior demonstrates the insertion of NH_4^+ ions and their extraction from the material. Notably, the corresponding peak at Point *a* can be attributed to the presence of NH_4^+ ions in NVO. The bands detected at 1111 and 959 cm^{-1} are characteristics of the stretching modes of V^{5+}═O and V^{4+}═O

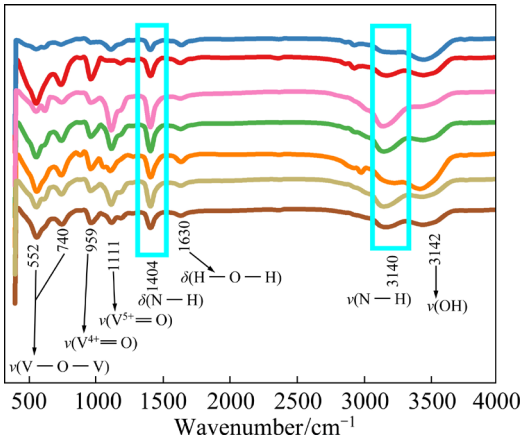

Fig. 7 Ex-situ FTIR spectra of NVO-2 under different discharge/charge conditions

groups, respectively, which correspond to the distorted VO_6 octahedral structures and VO_5 square pyramidal structures in NVO-2. During the discharge process, the intensity of the peak at 959 cm^{-1} initially increases due to the reversible reduction from V(V) to V(IV). However, this peak intensity then decreases during charging process, suggesting that V(IV) is reversibly oxidized back to V(V). The bands detected at 740 and 552 cm^{-1} can be ascribed to the asymmetric and symmetric stretching modes of the V—O—V bonds [27].

The ex-situ XPS spectra were acquired to investigate the surface chemistry states of the NVO-2 electrodes during the charge and discharge processes (Fig. 8). In the initial charged states, the V 2p spectra of the NVO-2 electrodes can be deconvoluted into contributions from V^{4+} at 516.8 eV and V^{5+} at 517.6 eV [28] (see Fig. 8(b)). As the system transitions from the initial state to the fully discharged state, the intensity of the V^{5+} peak

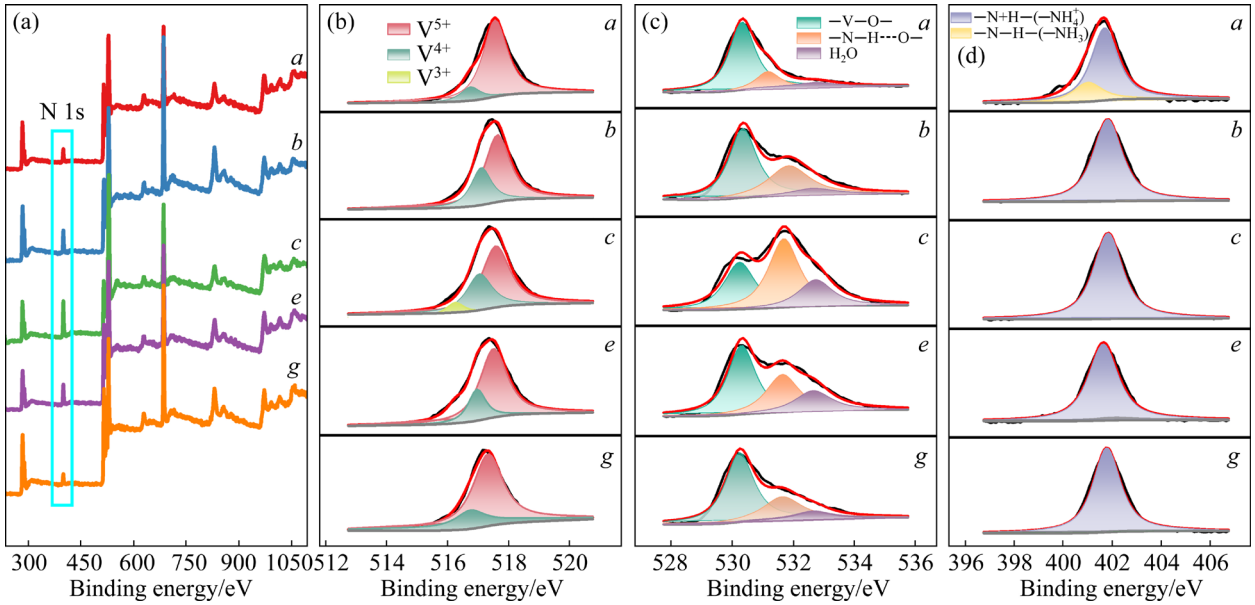

Fig. 8 XPS spectra of NVO-2 cycled to different potentials during GCD process (a); V 2p (b), O 1s (c), and N 1s (d) spectra of NVO-2 cycled to different potentials during GCD process

first decreases gradually and then increases, while that of the V^{4+} peak shows the opposite trend. When the battery is completely discharged at Point *c*, a new peak corresponding to V^{3+} at 516.3 eV can be observed. When fully charged, the valence state of V returns to its original state. The evolution of the valence state of V demonstrates the reversibility of the redox processes. Notably, the binding energies of both V^{4+} and V^{5+} shift to higher values (517.4 and 518.0 eV, respectively), which can be attributed to the intercalation of the NH_4^+ ions and the associated V^{4+}/V^{5+} bond rearrangements.

Moreover, the O 1s spectra (Fig. 8(c)) can be deconvoluted into three peaks at 530.3, 531.7, and 532.7 eV, which correspond to the V—O bonds between the NH_4^+ ions and the V—O layers, the —N—H···O bonds between the NH_4^+ ions and the H_2O molecules, and the H—O bonds within the H_2O molecules, respectively. As discharge occurs (from Point *a* to Point *c*), the area of the peak corresponding to the —N—H···O hydrogen bonds gradually increases with the insertion of the NH_4^+ ions. During the charging process, the peaks related to the —N—H···O hydrogen bonds remain, albeit with reduced areas. Several irreversibly embedded NH_4^+ ions can be observed to accumulate within the NVO lattice, and the irreversible migration of the NH_4^+ ions within the lattice leads to a reduction in the number of effective interaction sites, resulting in capacity attenuation [29,30]. During the discharge process, the presence of more H_2O molecules, which act as pillars and maintain the framework structure of the VO cathode material, enhances the mobility and reduces the diffusion resistance of the NH_4^+ ions [25,31−34]. The N 1s spectra exhibit two peaks at 399.7 and 401.5 eV (Fig. 8(d)), which correspond to —N—H— (—NH_3) and —N+H— (—NH_4^+), respectively [35−37]. These peaks are clearly visible in the pristine state and involve contributions from two distinct states of NH_4^+ ions. In both the charged and discharged states, the embedded NH_4^+ ions are present in the form of NH_4^+ ions.

3.4 Full cell performance

Among various anode materials, PANI is one of the most widely used conductive polymers owing to its easy availability, high electrical conductivity, exceptional electrochemical activity, and good stability. Herein, PANI was prepared via electro-polymerization and employed as the anode material. Compared with other polymers, PANI possesses a unique structure and can be doped with protonic acid through a non-redox process without any electron gain or loss [38]. Upon doping with protonic acid, protons bond with the N atoms present in the quinone ring in the PANI chain, leading to its reduction to a benzene ring structure.

Subsequently, anions enter the polymer, rendering it electrically neutral. Figure 9(a) demonstrates that PANI exists in three different oxidation states: leucoemeraldine (fully reduced), emeraldine (partially oxidized), and pernigraniline (fully oxidized) [39]. CV curves of CC@PANI electrodes at a scan rate of 5 mV/s (activated carbon was used as the counter electrode) are presented in Fig. S4 in Supporting Information. The differences among these oxidation states of PANI can be attributed to different proportions of quinone and benzene units within the PANI structure. Among these oxidation states, the half-oxidation state obtained at 50% protonic acid doping exhibits higher conductivity [40]. The emerald-green PANI used in this study, which was electrically polymerized via CV in the potential range from −0.5 to 1.5 V, was in a partially oxidized state. Figures 9(b, c) present the SEM images of PANI, which show that the PANI particles are uniformly distributed on the CC. The entire surface of the carbon fibers is covered with a dense and uniform layer of PANI.

Figure 10 depicts the CV curves of PANI deposited on a CC electrode after three cycles. Two reversible redox peaks, A_1 and D_1, are observed in the potential ranges of 300−480 and 580−600 mV, respectively. These peaks can be attributed to the oxidation of PANI. Peak A_1 corresponds to the transition from a fully reduced state to an intermediate oxidation state, while Peak D_1 represents the transition from an intermediate oxidation state to a fully oxidized state. Peaks A_2 and D_2 are associated with the reduction processes corresponding to these transitions [41]. Furthermore, two smaller redox peaks are visible in the ranges of 335−505 and 383−515 mV. These peaks are related to polymer degradation products. Peaks B_1 and B_2 represent the oxidation of benzoimine to benzoquinone, while Peaks C_1 and C_2 correspond to the redox peaks of benzoquinone and hydroquinone at slightly higher potentials, respectively [42].

FTIR spectroscopy measurements (Fig. 11(a)) reveal the presence of vibrational bands at 1563 and 1472 cm^{-1}, which are attributed to the C═C stretching vibrations of the quinone and benzene rings, respectively. The bands observed at 1301 and 1233 cm^{-1} can be attributed to the C—N stretching vibrations associated with the quinone and benzene structures. Furthermore, a vibration mode of quinone is observed at 1133 cm^{-1}. The band detected at 812 cm^{-1} corresponds to the out-of-plane bending vibrations of the C—H bonds in 1,4-substituted benzene rings [43−45]. Several diffraction peaks and lines are observed in the angular range from 10° to 31° (Fig. 11(b)), indicating the semi-crystalline nature of PANI. The diffraction line centered at 18.3° can be attributed to the (100) reflection of PANI, indicating a periodic arrangement parallel and perpendicular to the PANI chain. The diffraction peak centered at 25.7° is attributed to the (200) plane of orthorhombic PANI, indicating the interplanar spacing of PANI chains [46]. Furthermore, the XPS spectra reveal the presence of peaks corresponding to the C, N, O, and S elements, providing additional evidence for the formation of PANI (Fig. 11(c)).

Based on the above-mentioned results, a rocking-chair aqueous ammonium-ion full cell was constructed using NVO as the cathode material, PANI as the anode material, and $(NH_4)_2SO_4$ solution (1 mol/L) as the electrolyte (Fig. 12(a)). During the initial charging process, ammonium ions are intercalated into the PANI anode from the electrolyte, while the NVO cathode material undergoes a reduction from the V^{5+} state to V^{3+}/V^{4+}

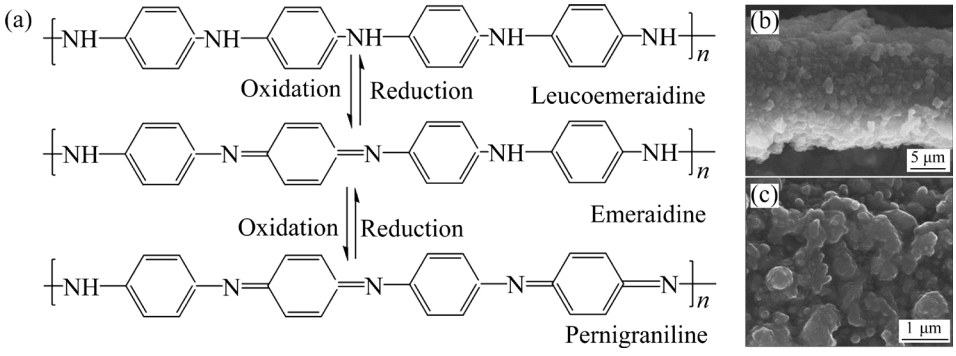

Fig. 9 Different oxidation states of PANI (a) and SEM images of PANI (b, c)

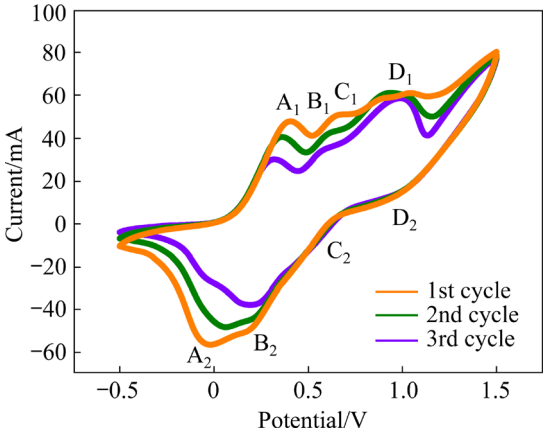

Fig. 10 CV curves of PANI deposited via electrochemical polymerization on CC

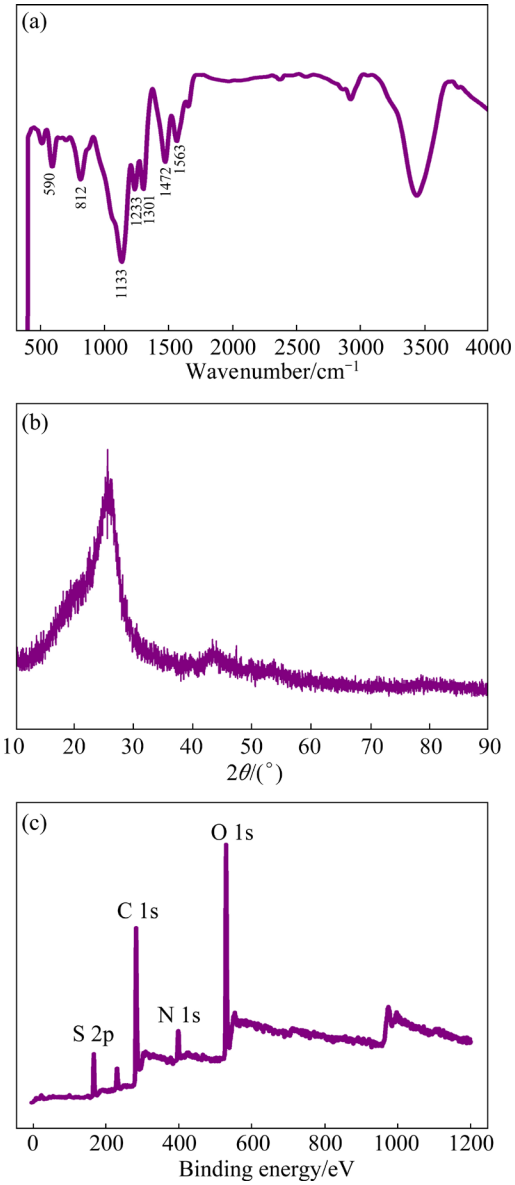

Fig. 11 FTIR spectrum (a), XRD pattern (b), and XPS spectrum (c) of PANI

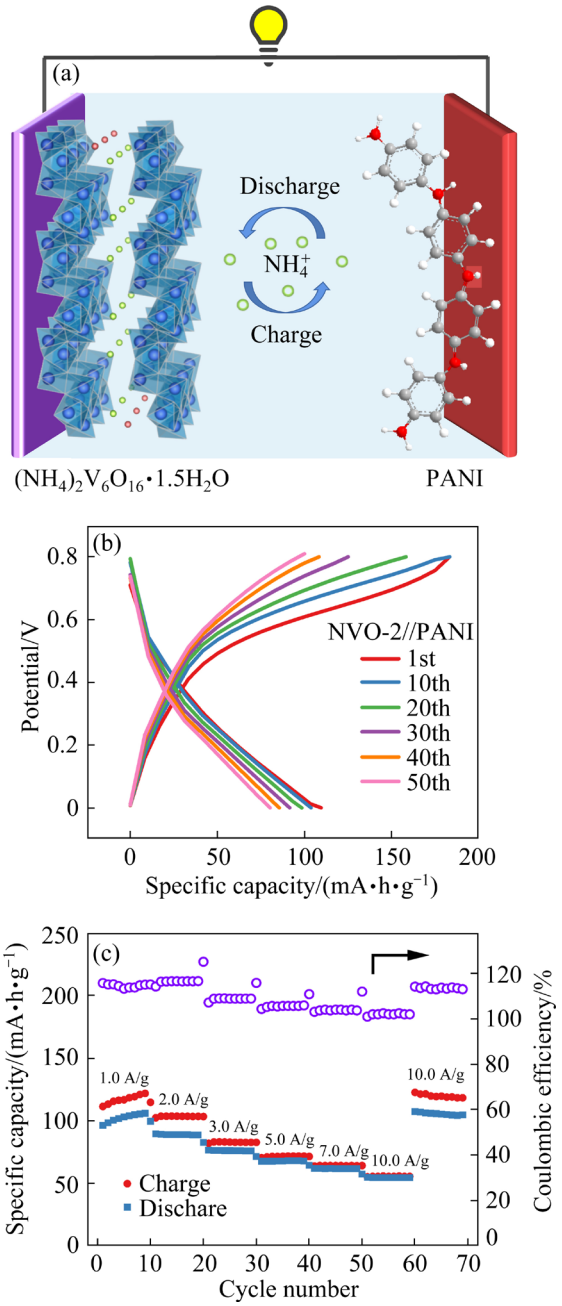

Fig. 12 Schematic of NVO//PANI full cell (a), GCD curves for different cycles (b), and rate performance at current densities of 1−10 A/g (c)

state. Conversely, during the discharge process, ammonium ions are extracted from PANI and inserted into the NVO cathode. In subsequent cycles, the NVO-2//PANI full cell sustains the rocking-chair mechanism for ammonium ions. The GCD curves of the NVO-2//PANI full cell are presented in Fig. 12(b). The initial specific capacity of the full cell was found to be 109.5 mA·h/g at a current density of 1.0 A/g, with an average operating voltage of 0.8 V, and the energy density

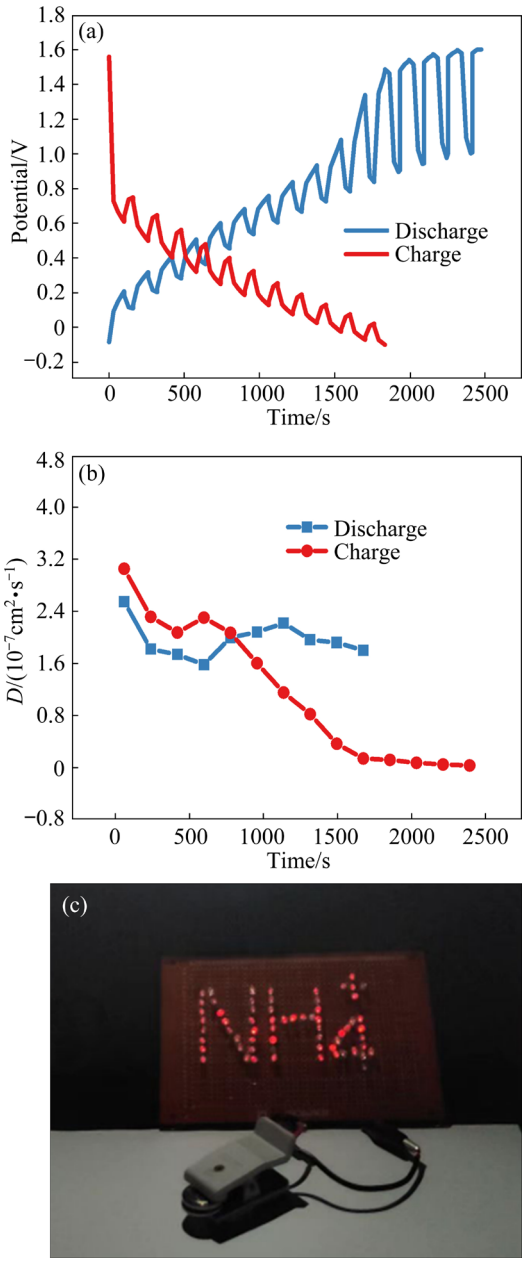

Fig. 13 Charge–discharge curves of NVO-2 cathode obtained via GITT (a), NH_4^+-ion diffusion coefficient during second cycle (b), and LED array powered by NVO-2//PANI full cell (c)

was approximately 23 W·h/kg. The as-prepared electrode material in this study exhibits several advantages in terms of electrochemical performance compared with other reported ammonium-ion cathode materials (Table S1 in Supporting Information). The discharge profile reveals the presence of a sloping voltage plateau between 0.2 and 0.5 V, while the charge profile shows a sloping plateau within the range from 0.6 to 0.75 V. The NVO-2//PANI full cell exhibits specific capacities of 102.9, 88.8, 76.1, 71.5, and 64.2 mA·h/g at current densities of 1.0, 2.0, 3.0, 5.0, and 7.0 A/g, respectively, indicating good rate capability. Moreover, when the current density is abruptly reduced to 1.0 A/g, the full cell is capable of recovering a reversible capacity of 105.1 mA·h/g (Fig. 12(c)).

To better comprehend the electrochemical behavior of NVO-2//PANI full cell, the galvanostatic intermittent titration technique (GITT) was employed to investigate the ammonium-ion diffusion kinetics of this cell during the second cycle (Figs. 13(a, b)). The estimated ammonium-ion diffusion coefficient ($D_{NH_4^+}$) was approximately 5.5×10^{-7} cm^2/s. A relatively stable trend can be observed throughout the GITT cycle, indicating fast and stable diffusion behavior. Figure 13(c) displays an array of light-emitting diodes (LEDs) powered by an NVO-2//PANI full cell to spell "NH_4^+". These results demonstrate the practical application potential of the devices developed in this study.

4 Conclusions

(1) The NVO nanoribbons have a layered structure and large interlayer spacing and they are intrinsic sources for NH_4^+ ions. Therefore, the NVO cathodes have enhanced electrochemical behavior.

(2) The hydrogen bonding interactions and surface free energies vary with the pH of the growth solution, leading to differences in the composition and morphological characteristics of the obtained ammonium vanadate. This affects the electrochemical properties of the NVO cathodes.

(3) Based on the synergy between PANI and NVO, the prepared ammonium-ion full cell with NVO as the cathode and PANI grown on CC as the anode, exhibits a discharge capacity of 109.5 mA·h/g, energy density of 23 W·h/kg, excellent rate capability, and fast ion diffusion kinetics.

CRediT authorship contribution statement

Lin XING: Methodology, Data curation, Writing − Original draft; **Wei ZHOU:** Software, Data curation, Writing − Review & editing, Investigation; **Kai-xiong XIANG:** Investigation, Funding acquisition; **Wei-na DENG**, **Liang CHEN**, **Hai ZHU:** Conceptualization, Supervision, Writing – Review & editing; **Han CHEN:** Project management, Financial support for experiments, Preparation of experimental reagents and materials, Experimental exploration.

Declaration of competing interest

The authors declare that they have no known competing financial interests or personal relationships that could have appeared to influence the work reported in this paper.

Acknowledgments

This work was supported by the National Natural Science Foundation of China (Nos. 52171200, 52371211) and the Changsha Special Project, China (No. kh2301006).

Supporting Information

Supporting Information in this paper can be found at: http://tnmsc.csu.edu.cn/download/19-p1292-2023-0835-Supporting_Information.pdf.

References

[1] TAN Hui-teng, XU Lian-hua, GENG Hong-bo, RUI Xian-hong, LI Cheng-chao, HUANG Shao-ming. Nanostructured $Li_3V_2(PO_4)_3$ cathodes [J]. Small, 2018, 14(21): 1800567−1800588.

[2] TANG Wei, ZHU Yu-song, HOU Yu-yang, LIU Li-li, WU Yu-ping, LOH Kian-ping, ZHANG Han-ping, ZHU Kai. Aqueous rechargeable lithium batteries as an energy storage system of superfast charging [J]. Energy & Environmental Science, 2013, 6: 2093−2104.

[3] YANG Jian, ZHOU Yuan, ZHANG Zong-liang, XU Kai-hua, ZHANG Kun, LAI Yan-qing, JIANG Liang-xing. Effect of electric field on leaching valuable metals from spent lithium-ion batteries [J]. Transactions of Nonferrous Metals Society of China, 2023, 33: 632−641.

[4] QIN Mu-lan, YIN Chang-yu, XU Wen, LIU Yang, WEN Jun-hao, SHEN Bin, WANG Wei-gang, LIU Wan-min. Facile synthesis of high capacity P2-type $Na_{2/3}Fe_{1/2}Mn_{1/2}O_2$ cathode material for sodium-ion batteries [J]. Transactions of Nonferrous Metals Society of China, 2021, 31: 2074−2080.

[5] PASTA M, WESSELLS C D, HUGGINS R A, CUI Yi. A high-rate and long cycle life aqueous electrolyte battery for grid-scale energy storage [J]. Nature Communications, 2012, 3(1): 1149−1155.

[6] LIU Zhen, HE Han-bing, LUO Ze-xiang, WANG Xiao-feng, ZENG Jing. 3D printing of customized MnO_2 cathode for aqueous zinc-ion batteries [J]. Transactions of Nonferrous Metals Society of China, 2023, 33: 1193−1204.

[7] WEI Lu-yao, LIAN Ru-qian, WANG Da-shuai, ZHAO Ying-ying, YANG Di, ZHAO Hai-nan, WANG Yi-zhan, CHEN Gang, WEI Ying-jin. Magnesium ion storage properties in a layered $(NH_4)_2V_6O_{16}\cdot 1.5H_2O$ nanobelt cathode material activated by lattice water [J]. ACS Applied Materials & Interfaces, 2021, 13: 30625−30632.

[8] PONROUCH A, FRONTERA C, BARDE F, PALACíN M R. Towards a calcium-based rechargeable battery [J]. Nature Materials, 2015, 15(2): 169−172.

[9] WANG Hua-li, BAI Ying, CHEN Shi, LUO Xiang-yi, WU Chuan, WU Feng, LU Jun, AMINE K. Binder-free V_2O_5 cathode for greener rechargeable aluminum battery [J]. ACS Applied Materials & Interfaces, 2015, 7: 80−84.

[10] WESSELLS C D, PEDDADA S V, MCDOWELL M T, HUGGINS R A, CUI Yi. The effect of insertion species on nanostructured open framework hexacyanoferrate battery electrodes [J]. Journal of the Electrochemical Society, 2011, 159(2): A98.

[11] XING Jun-jie, FU Xiu-li, GUAN Shun-dong, ZHANG Yu, LEI Ming, PENG Zhi-jian. Novel K−V−Fe Prussian blue analogues nanocubes for high-performance aqueous ammonium ion batteries [J]. Applied Surface Science, 2021, 543: 148843−148850.

[12] LUKATSKAYA M R, MASHTALIR O, REN C E, DALL'AGNESE Y, ROZIER P, TABERNA P L, NAGUIB M, SIMON P, BARSOUM M W, GOGOTSI Y. Cation intercalation and high volumetric capacitance of two-dimensional titanium carbide [J]. Science, 2013, 341: 1502−1505.

[13] KUCHENA S F, WANG Ying. Superior polyaniline cathode material with enhanced capacity for ammonium ion storage [J]. ACS Applied Energy Materials, 2020, 3: 11690−11698.

[14] HOLOUBEK J J, JIANG Heng, LEONARD Dl P, QI Yi-tong, BUSTAMANTE G C, JI Xiu-lei. Amorphous titanic acid electrode: Its electrochemical storage of ammonium in a new water-in-salt electrolyte [J]. Chemical Communications, 2018, 54: 9805−9808.

[15] DONG Sheng-yang, SHIN W, JIANG Heng, WU Xian-yong, LI Zhi-fei, HOLOUBEK J, STICKLE W F, KEY B, LIU Cong, LU Jun, GREANEY P A, ZHANG Xiao-gang, JI Xiu-lei. Ultra-fast NH_4^+ storage: Strong H bonding between NH_4^+ and Bi-layered V_2O_5 [J]. Chem, 2019, 5: 1537−1551.

[16] LIANG Guo-jin, WANG Yan-lei, HUANG Zhao-dong, MO Fu-nian, LI Xin-liang, YANG Qi, WANG Dong-hong, LI Hong-fei, CHEN Shi-mou, ZHI Chun-yi. Initiating Hexagonal MoO_3 for superb-stable and fast NH_4^+ storage based on hydrogen bond chemistry [J]. Advanced Materials, 2020, 32: 1907802.

[17] WU Xian-yong, QI Yi-tong, HONG J J, LI Zhi-fei, HERNANDEZ A S, JI Xiu-lei. Rocking-chair ammonium-ion battery: A highly reversible aqueous energy storage system [J]. Angewandte Chemie International Edition, 2017, 56: 13026−13030.

[18] SIDEY V. On the effective ionic radii for ammonium [J]. Acta Crystallographica Section B, 2016, 72: 626−633.

[19] JIANG Han-mei, ZHANG Yi-fu, PAN Zheng-hui, XU Lei, ZHENG Ji-qi, GAO Zhan-ming, HU Tao, MENG Chang-gong. Facile hydrothermal synthesis and electrochemical properties of $(NH_4)_2V_{10}O_{25}\cdot 8H_2O$ nanobelts for high-performance aqueous zinc ion batteries [J]. Electrochimica Acta, 2020, 332: 135506.

[20] WAN Fang, ZHANG Lin-lin, DAI Xi, WANG Xin-yu, NIU Zhi-qiang, CHEN Jun. Aqueous rechargeable zinc/sodium vanadate batteries with enhanced performance from simultaneous insertion of dual carriers [J]. Nature Communications, 2018, 9(1): 1656−1666.

[21] WANG Nian, CHEN Wen, MAI Li-qiang, DAI Ying. Selected-control hydrothermal synthesis and formation

mechanism of 1D ammonium vanadate [J]. Journal of Solid State Chemistry, 2008, 181: 652−657.

[22] ZENG Gui-lin, WANG Yu-qiu, LOU Xiao-ming, CHEN Han, JIANG Shao-hua, ZHOU Wei. Vanadium oxide/carbonized chestnut needle composites as cathode materials for advanced aqueous zinc-ion batteries [J]. Journal of Energy Storage, 2024, 77: 109859−109868.

[23] TANG Bo-ya, ZHOU Jiang, FANG Guo-zhao, LIU Fei, ZHU Chu-yu, WANG Chao, PAN An-qiang, LIANG Shu-quan. Engineering the interplanar spacing of ammonium vanadates as a high-performance aqueous zinc-ion battery cathode [J]. Journal of Materials Chemistry A, 2019, 7: 940−945.

[24] MA Shu-ci, SHI Xiao-dong, LIU Zhe-xuan, ZHOU Yi-fan, WANG Pin-ji, ZHOU Jiang, LIANG Shu-quan. PVDF−HFP binder for advanced zinc−manganese batteries [J]. Transactions of Nonferrous Metals Society of China, 2022, 32: 3005−3014.

[25] WEI Tong-ye, LI Qian, YANG Gong-zheng, WANG Cheng-xin. Highly reversible and long-life cycling aqueous zinc-ion battery based on ultrathin $(NH_4)_2V_{10}O_{25}\cdot 8H_2O$ nanobelts [J]. Journal of Materials Chemistry A, 2018, 6: 20402−20410.

[26] HU Fang, GU Yao, CUI Fu-han, SONG Gui-hong, ZHU Kai. High-performance $(NH_4)_2V_6O_{16}\cdot 0.9H_2O$ nanobelts modified with reduced graphene oxide for aqueous zinc ion batteries [J]. Chinese Chemical Letters, 2021, 32: 3793−3798.

[27] MAI L Q, LAO C S, HU B, ZHOU J, QI Y Y, CHEN W, GU E D, WANG Z L. Synthesis and electrical transport of single-crystal $NH_4V_3O_8$ nanobelts [J]. ChemInform, 2006, 37: 18138−18141.

[28] SILVERSMIT G, DEPLA D, POELMAN H, MARIN G B, GRYSE R D. Determination of the V 2p XPS binding energies for different vanadium oxidation states (V^{5+} to V^{0+}) [J]. Journal of Electron Spectroscopy and Related Phenomena, 2004, 135: 167−175.

[29] BIN Duan, LIU Yao, YANG Bei-bei, HUANG Jian-hang, DONG Xiao-li, ZHANG Xiao, WANG Yong-gang, XIA Yong-yao. Engineering a high-energy-density and long lifespan aqueous zinc battery via ammonium vanadium bronze [J]. ACS applied Materials Interfaces, 2019, 23: 20796−20803.

[30] LAI Jian-wei, TANG Hui, ZHU Xiu-ping, WANG Ying. A hydrated NH V_3O_8 nanobelt electrode for superior aqueous and quasi-solid-state zinc ion batteries [J]. Journal of Materials Chemistry A, 2019, 7: 23140−23148.

[31] HU Ping, ZHU Ting, WANG Xuan-peng, WEI Xiu-juan, YAN Meng-yu, LI Jian-tao, LUO Wen, YANG Wei, ZHANG Wen-cui, ZHOU Liang, ZHOU Zhi-qiang, MAI Li-qiang. Highly durable $Na_2V_6O_{16}\cdot 1.63H_2O$ nanowire cathode for aqueous zinc-ion battery [J]. Nano Letters, 2018, 18: 1758−1763.

[32] LIU Chao-feng, NEALE Z, ZHENG Ji-qi, JIA Xiao-xiao, HUANG Juan-juan, YAN Meng-yu, TIAN Meng, WANG Ming-shan, YANG Ji-hui, CAO Guo-zhong. Expanded hydrated vanadate for high-performance aqueous zinc-ion batteries [J]. Energy & Environmental Science, 2019, 12: 2273−2285.

[33] ZHANG Ning, DONG Yang, JIA Ming, BIAN Xu, WANG Yuan-yuan, QIU Man-de, XU Jian-zhong, LIU Yong-chang, JIAO Li-fang, CHENG Fang-yi. Rechargeable aqueous $Zn-V_2O_5$ battery with high energy density and long cycle life [J]. ACS Energy Letters, 2018, 3(6): 1366−1372.

[34] TRIKALITIS P N, PETKOV V, KANATZIDIS M G. Structure of redox intercalated $(NH_4)_{0.5}V_2O_5\cdot mH_2O$ Xerogel using the pair distribution function technique [J]. Chemistry of Materials, 2003, 15: 3337−3342.

[35] MENG Xing, WANG Hai-Ning, WANG Xiao-Kun, DONG Long-Zhang, ZOU Yan-Hong. Cations mediating proton conductivity in an oxalate based microporous coordination polymer [J]. New Journal of Chemistry, 2019, 43(1): 24−27.

[36] SHI Xiao-Hui, CHEN Li, LIU Bo-Wen, LONG Jia-Wei, XU Ying-Jun, WANG Yu-Zhong. Carbon fibers decorated by polyelectrolyte complexes toward their epoxy resin composites with high fire safety [J]. Chinese Journal of Polymer Science, 2018, 36: 1375−1384.

[37] SARKAR T, KUMAR P, BHARADWAJ M D, WAGHMARE U. Structural transformation during Li/Na insertion and theoretical cyclic voltammetry of the δ-$NH_4V_4O_{10}$ electrode: A first-principles study [J]. Physical Chemistry Chemical Physics, 2016, 18: 9344−9348.

[38] GHANBARI K, MOUSAVI M F, SHAMSIPUR M, KARAMI H. Synthesis of polyaniline/graphite composite as a cathode of Zn-polyaniline rechargeable battery [J]. Journal of Power Sources, 2007, 170: 513−519.

[39] BAKER C O, HUANG Xin-wei, NELSON W, KANER R B. Polyaniline nanofibers: Broadening applications for conducting polymers [J]. Chemical Society Reviews, 2017, 46(5): 1510−1525.

[40] LUO Ya-ni, GUO Rui-song, LI Ting-ting, LI Fu-yun, LIU Zhi-chao, ZHENG Mei, WANG Bao-yu, YANG Zhi-wei, LUO Hong-lin, WAN Yi-zao. Application of polyaniline for Li-ion batteries, lithium−sulfur batteries, and supercapacitors [J]. ChemSusChem, 2019, 12(8): 1591−1611.

[41] CUI C Q, ONG L H, TAN T C, LEE J Y. Extent of incorporation of hydrolysis products in polyaniline films deposited by cyclic potential sweep [J]. Electrochimica Acta, 1993, 38(10): 1395−1404.

[42] STILWELL D E, PARK S M. Electrochemistry of conductive polymers: II. Electrochemical studies on growth properties of polyaniline [J]. Journal of the Electrochemical Society, 1988, 135(9): 2254.

[43] YU Ting-ting, YANG Ren-jie, ZHAO Xiang-yu, SHEN Xiao-dong. Polyaniline-intercalated FeOCl cathode material for chloride-ion batteries [J]. ChemElectroChem, 2019, 6(6): 1761−1767.

[44] ZHAO Zhi-gang, YU Ting-ting, MIAO Ying-chun, ZHAO Xiang-yu. Chloride ion-doped polyaniline/carbon nanotube nanocomposite materials as new cathodes for chloride ion battery [J]. Electrochimica Acta, 2018, 270: 30−36.

[45] MO Liu-ye, ZHENG Hai-tao. Solid coated $Li_4Ti_5O_{12}$ (LTO) using polyaniline (PANI) as anode materials for improving thermal safety for lithium ion battery [J]. Energy Reports, 2020, 6: 2913−2918.

[46] MOSTAFA N Y, MOHAMED M B, IMAM N G, ALHAMYANI M, HEIBA Z K. Electrical and optical properties of hydrogen titanate nanotube/PANI hybrid nanocomposites [J]. Colloid and Polymer Science, 2016, 294: 215−224.

$(NH_4)_2V_6O_{16}·1.5H_2O$ 纳米带的制备及其在水系铵离子电池中的应用

幸 琳[1,2]，周 伟[1]，向楷雄[2]，邓伟娜[1]，陈 亮[1]，朱 海[1]，陈 晗[1]

1. 长沙学院 环境光催化应用湖南省重点实验室，长沙 410022；
2. 湖南工业大学 醴陵陶瓷学院，株洲 412007

摘 要：为了构建高性能水系铵离子电池，采用水热法，通过调节反应体系的 pH 值，制备了$(NH_4)_2V_6O_{16}·1.5H_2O$ (NVO)纳米带正极，并在碳布上生长聚苯胺(PANI)活性材料制备了负极。组装的 NVO//PANI 电池在 1.0 A/g 的电流密度下表现出 109.5 mA·h/g 的可逆容量和 23 W·h/kg 的高能量密度。铵离子的嵌入/脱嵌机制主要由赝电容行为决定。这些结果表明，NVO 是一种潜在的水系铵离子电池正极候选材料。

关键词：$(NH_4)_2V_6O_{16}·1.5H_2O$；正极；铵离子电池；碳布；电化学性能

(Edited by Bing YANG)